UNIVERSITYOF
BIRMINGHAM

A closed-loop linear engine generator using inert gases

Li, Mingqiang; Ngwaka, Ugochukwu; Moeini Korbekandi, Ramin; Baker, Nick; Wu, Dawei; Tsolakis, Athanasios

[Link to publication on Research at Birmingham portal](#)

A closed-loop linear engine generator using inert gases: A performance and exergy study

Mingqiang Li [a], Ugochukwu Ngwaka [a], Ramin Moeini Korbekandi [b], Nick Baker [b], Dawei Wu [a,*], Athanasios Tsolakis [a]

[a] *Department of Mechanical Engineering, University of Birmingham, B15 2TT, United Kingdom*
[b] *School of Engineering, Newcastle University, NE1 7RU, United Kingdom*

A B S T R A C T

This paper introduces air, argon, and helium used as working fluids in a first-of-its-kind closed-loop Linear Engine Generator (LEG) to reveal its performance map, energy flow, exergy destruction, and exergy efficiency. Properties of the working fluids affect the LEG designs, e.g., compression ratio and applicable temperature range, in turn, impacting system efficiency and power output. A comparison is made between open-loop and closed-loop models using air at a peak temperature below 1095 K, based on a laboratory prototype of an open-loop LEG. The closed-loop models using air, argon, and helium achieve impressive efficiencies of 43.92%, 43.74%, and 51.30%, respectively, at the intake pressure of 0.85 bar and intake temperature of 225 K. The LEG using air shows the highest power output of 2448 W, while the helium version generates 2044 W and the argon version 1850 W. The exhaust energy loss is one of the major energy losses, which is comparable to the mechanical power output, while the friction loss ranges from 7.4% to 9.3%. The compressor and expander have low exergy destructions and high exergy efficiencies of more than 96%. In the closed-loop systems, the maximum exergy destruction rate is seen at the condenser affected by the coolant's low temperature.

1. Introduction

Given the urgent challenges posed by global climate change, the energy crisis [1], and stringent emissions regulations [2], it is imperative to explore alternative engine designs that are more environmentally friendly and flexible in terms of utilizing various renewable energy forms effectively. In this context, closed-loop engines have gained significant attention due to their potential to adapt to different heat addition methods, improve system efficiency, reduce carbon emissions, and promote energy diversity [3].

Closed-loop engines operate in a closed thermodynamic cycle, achieving air independence through the recirculation of the working fluid within the engine. This mode of operation offers several advantages over open-loop engines: flexible use of waste heat and cooling energy (from cryogenic fuel evaporation); various working fluids such as air, carbon dioxide, helium, or other inert gases; different fuels to be used in their optimal conditions with easier emission treatments; no need to filter incoming air in a polluted environment [4]. Researchers have reviewed closed-loop engines in the technological aspects,

operating characteristics, applications, and commercial development, including the closed-loop gas turbine [4], closed-loop diesel engine [5], and closed-loop Stirling engine [6]. Stirling engine is the most typical and widely studied type although it still faces several development challenges: long response times to speed [7], power requirements affected by the external combustion and the use of regenerators [8], side thrust, and large mechanical friction from the crankshaft, complex design [9], unstable operation for the non-crankshaft version [10], and no active control for no valve mechanism [11].

Nevertheless, there is ongoing interest in further exploring various types of closed-loop engines. The linear engine generator (LEG) was proposed as an open-loop Joule cycle engine working in various configurations and thermodynamic cycles [12], which incorporates a free piston engine setup and a linear generator. Modifications could be made to the LEG to convert it to a closed-loop configuration, which uses a cooler or a condenser to expel heat from the engine cycle. The closed-loop LEG may share the same advantages of high-power density, a compact layout, mechanical simplicity, reduced friction losses, fewer moving parts, and energy source flexibility as the open-loop counterparts [13]. Additionally, the closed-loop LEG may have low emission

Abbreviations

Ar	Argon
BMEP	Brake Mean Effective Pressure
CR	Compression ratio
EMF	Electromotive force
He	Helium
HTHE	High temperature heat exchanger
LEG	Linear engine generator
LG	Linear generator
LJEG	Linear Joule Engine Generator
OBDC	Operation Bottom Dead Center
OTDC	Operation Top Dead Center
PM	Permanent magnet
STP	Standard temperature and pressure

Nomenclature

a_m	Friction force parameter $(-)$
a_n	Friction force parameter $(-)$
A	Orifice area (m^2)
c_p	Specific heat capacity at constant pressure $(J/\ (kg \bullet K))$
$\dot{C}$	Heat capacity rate $(J/(s \bullet K))$
D_b	Bore diameter (m)
E	Energy (J)
$E_{x,i}$	Exergy destruction (J)
f_d	Coulomb friction force (N)
f_{dp}	Pressure friction coefficient $(-)$
f_s	Stiction force (N)
h	Specific enthalpy (kJ/kg)
H	Enthalpy (kJ)
i	Exergy destruction rate (W)
I	Current (A)
k	The specific heat ratio $(-)$
k_g	Thermal conductivity of gases $(W/(m \bullet K))$

L_i	The constant value of inductance (H)
m	Working fluid mass (kg)
$\dot{m}$	Mass flow rate (kg/s)
N	Turns of the coil per phase $(-)$
P	Pressure (pa)
Q	Heat (J)
R	Ideal gas constant $(J/(mol \bullet K))$
R_e	Load resistance (Ω)
R_g	Specific gas constant $(J/(kg \bullet K))$
s	Specific entropy $(J/(kg \bullet K))$
S	Entropy (J/K)
T	Temperature (K)
U	Internal energy (J)
v_g	Absolute viscosity (cP)
V	Volume (m^3)
V_E	Voltage for the external load (V)
V_L	Induced voltage (V)
V_r	Voltage of the coil resistance (V)
W	Work (J)
W_p	Thickness of the piston ring (m)
W_s	Work per cycle (J)
x	Distance (m)
$\dot{x}$	Velocity (m/s)
$\ddot{x}$	Acceleration (m/s^2)
α	Ratio of the bores $(-)$
η	Engine thermal efficiency $(-)$
η_x	Exergy efficiency $(-)$
μ	Fluid dynamic viscosity $(pa \bullet s)$
π	Pressure ratio $(-)$
ρ	Density (kg/m^3)
φ	Magnetic flux $(Weber)$
ψ_i	Flux linkage due to current $(Weber)$

characteristics, as seen in other closed-loop systems using solar energy [14] and biofuel [15], and can utilize net zero carbon heat sources, such as green hydrogen [16], and ammonia [17]. The closed-loop LEG may find its applications in micro-cogeneration [18] and the marine sector [19].

Investigations into free piston engines or similar setups as LEG have been conducted over the years. In 1998, Blarigan et al. [20] examined a free-piston linear generator similar to the LEG and used homogeneous charge compression ignition to test various fuels, including renewable fuels such as hydrogen. In 1998 and 1999, Clark et al. [21] designed and tested a two-stroke spark-ignited linear engine alternator under several different operating modes. Similarly, in 2015, Jia et al. [22] studied the starting and steady processes of a dual-piston free-piston engine generator. All the engines mentioned above focused on internal combustion LEGs, where the movement of the piston system affects the combustion performance effectively and mutually. The open-loop Joule cycle LEG was proposed in 2012 for cogeneration applications [18] and avoided in-cylinder internal combustion to adapt the LEG to various combustion technologies, fuels, and a more flexible layout. An open-loop prototype test rig with the dynamic and thermodynamic model was presented in 2018 [23]. The dry friction model was developed in 2019 [24], and the coupled engine parametric studies were presented in 2021 [25]. The researcher's team is currently testing a lab-size prototype using the open-loop Joule Cycle [19].

Studies on closed-loop engines have demonstrated the potential of various working fluids, such as helium [26], nitrogen [26], argon [27], hydrogen [28], and CO_2 [29] in improving engine performance. The existing research on the Joule cycle LEG has been focused on open-loop

cycles, while a single work reported a semi-closed loop [25]. This paper investigates a new compact closed-loop LEG design to address this gap. The study aims to explore the potential of air, argon, and helium as working fluids in closed-loop configuration and how they influence the engine parameters like compression ratio and applicable temperature range, which affect system performance. This paper also investigates the impact of intake pressure and temperature on the closed-loop LEG configuration, taking into account the influence of pressure [30] and temperature [31] on the gas turbine engine performance and the potential of using cold energy from fuel storage to boost cycle efficiency. The results of this study systematically compare the closed-loop system with the open-loop LEG with the aforementioned working fluids. Detail engine maps, energy flow analysis, and exergy destruction and efficiency of the open and closed-loop systems were conducted from a thermodynamic perspective.

2. System description

The open-loop lab-scale Joule cycle LEG prototype has a symmetrical configuration as shown in Fig. 1 (a), and it has a compressor and an expander on both sides of the linear generator (LG). Based on the prototype, Fig. 1 (b). Depicts the new open-loop Joule cycle LEG, which modified the separated compressors to be a double-acting compressor, which helps engine compactness. The main components also include an external combustor or high-temperature heat exchanger (HTHE), and the poppet valve actuation systems. Poppet valves control the expander gas exchange, and the poppet valves are controlled by a specially designed in-house actuation system driven by voice coil motors in the
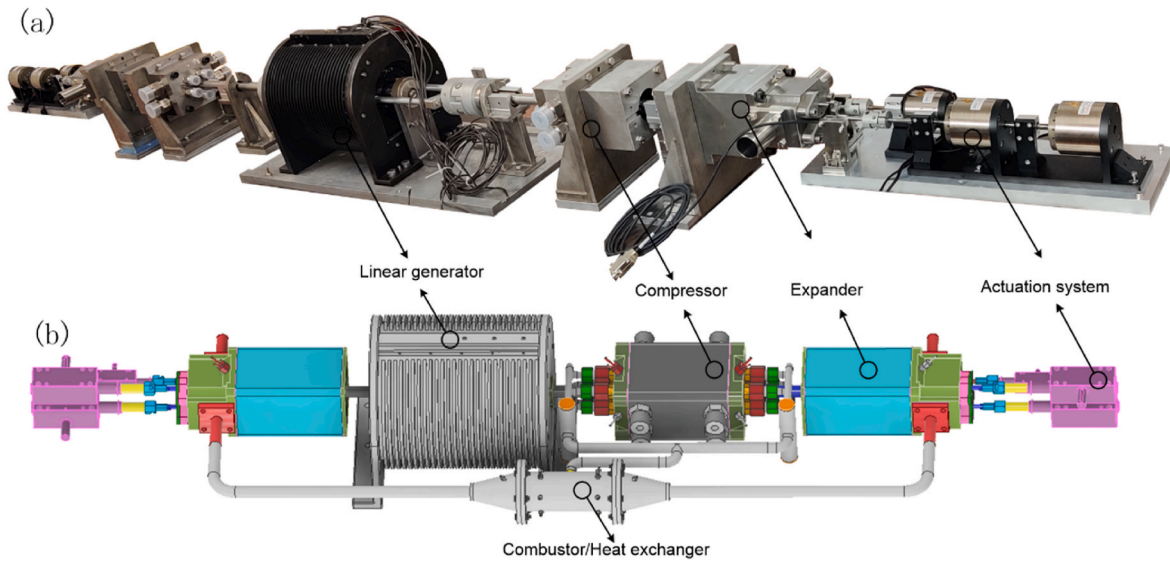
Fig. 1. (a) The Lab-scale LEG prototype and (b) schematic diagram of the modified open-loop Joule cycle LEG.

prototype.

The specifications of the prototype, and the open-loop and closed-loop LEG models are shown in Table 1. Every component of the LEG prototype was designed to reach favorable performance within the constraints of mechanical configuration and material properties, and the details are presented in Ref. [19]. Fig. 2 depicts the closed-loop version of the LEG, with an HTHE and a condenser to form a closed-loop configuration. In fact, the condenser here is a low-temperature heat exchanger, with low-temperature hydrogen serving as the coolant. The HTHE is a plate mini-channel heat exchanger for its high-temperature endurance of up to 1273 K, and the effectiveness is 0.9 [32]; the air is used as a hot side fluid [33]. Additionally, in the LEG models, the temperature before the expanders is limited to 1095 K due to constraints related to the materials used in the system.

3. Methodology

3.1. LEG model

For both open-loop and closed-loop LEGs, the dynamics of the mover (connecting rod, pistons, and LG translator) are calculated using Newton's second law. The force layout of the mover during a right stroke is shown in Fig. 3.

The positive forces (marked by the red arrow) include forces from the left expander and the left side of the compressor. The other forces are all opposing forces (marked by a green arrow). The force balance equation describing the system is expressed in Equation (1) [24]:

$$m\frac{dx^2}{dt^2} = F_{exp,L} + F_{comp,L} + F_{exp,R} + F_{Comp,R} + F_{magnetic} + F_{fri} \quad (1)$$

where x is the displacement, m is the total mass of the mover, and

Table 1
Engine specifications for the prototype and models.

Engine name	Unit	LEG prototype and models
Bore diameter of compressor	[mm]	70
Bore diameter of expanders	[mm]	82
Stroke	[mm]	117
Compressor valve type	[−]	Check valve
Expanders valve type	[−]	Poppet valve
Moving mass	[kg]	17.5 for the prototype and 16.5 for the models

$F_{magnetic}$ denotes the magnetic force due to the linear generator. The subscripts exp and $comp$ mean expander and compressor, F_{gas} denotes the gas forces, and subscripts L, R, and fri represent the left side, right side, and friction. The gas force is calculated with Equation (2):

$$F_{exp,L}, F_{comp,L} = F_{gas} = P \bullet A \quad (2)$$

where P is the relevant chamber gas pressure and A is the cross-section area of the relevant piston.

The friction comes from the compressor and expander piston rings, and the bearing friction, and each friction component in Equation (3) is in three categories; dry friction (F_{fd}), viscous friction (F_{fv}), and the friction due to the pressure loading (F_{fp}) and the dry contact friction is expressed in Equation (4) [24]:

$$F_{fri} = F_{fd} + F_{fv} + F_{fp} \quad (3)$$

$$F_{fd} = \left[f_d + (f_s - f_d) \bullet \exp\left(-\frac{a_m \bullet |\dot{x}|}{|\ddot{x}| + a_n} \right) \right] \bullet sign(\dot{x}) \quad (4)$$

where f_d is the Coulomb friction force, f_s is the Stiction force, a_m and a_n are empirical parameters. The viscous friction force is expressed as $F_{fv} = C_f \bullet \dot{x}$, where C_f is viscous damping coefficient and $\dot{x}$ is the velocity [34]. Friction due to pressure loading force is expressed in Equation (5) [35]:

$$F_{fp} = f_{dp} \bullet \pi \bullet P_{dif} \bullet D_b \bullet w_p \quad (5)$$

where f_{dp} is the pressure friction coefficient, P_{dif} is the pressure difference between the cylinder chambers, and D_b is the bore diameter of the cylinder, w_p is the thickness of the piston rings.

The thermodynamic analysis is of a one-dimensional type, where the potential and kinetic energies of the system are not considered, and the ideal gas law is assumed when using a semi-perfect gas definition [36]. A polytropic hypothesis (Equation (6)) is used to reduce complexity and avoid the effect of insufficient data on thermal exchanges:

$$P \bullet V^k = \text{constant} \quad (6)$$

where k is the specific heat ratio, P is the pressure and V is the volume. Considering the ideal gas law, $P \bullet V = nRT$, Equation (6) is rewritten in Equation (7):

$$P^{1-k} \bullet T^k = \text{constant} \quad (7)$$

The first law of thermodynamics (Equation (8)) could describe the energy and mass changes in the compressor and expanders, which are
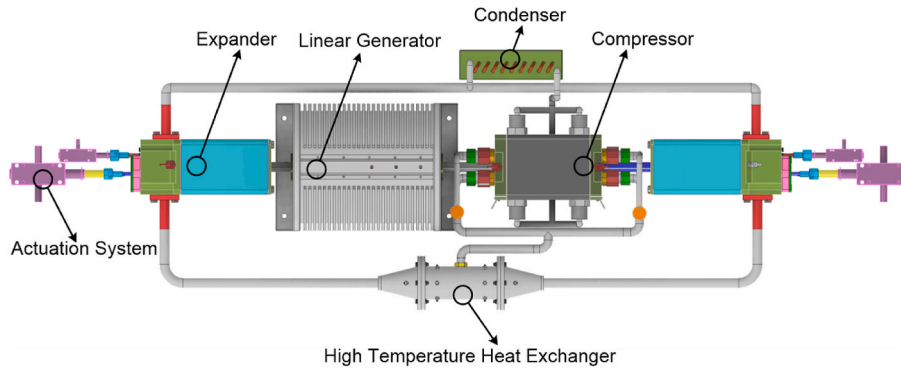
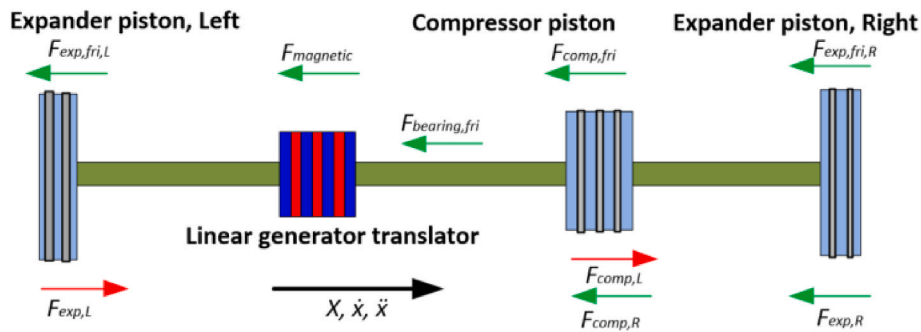**Fig. 2.** Schematic diagram of closed-loop Joule cycle LEG.

Fig. 3. Force layout on the mover.

variable volume chambers with heat transfer:

$$\frac{dU}{dt} = \sum \dot{m}_j \bullet h_j + \frac{dQ}{dt} - P \bullet \frac{dV}{dt} \tag{8}$$

where $\dot{m}$ is the mass flow rate, $\dot{m}_j \bullet h_j$ represents the enthalpy flow rate and subscript j represents working fluid flow. dQ/dt is the heat flow, provided by or exiting from the control volume, and dW/dt is the pressure work rate, P is the pressure and dV/dt is the volume change rate.

The thermodynamic processes of Joule cycle LEGs are shown in Fig. 10, and in the Joule cycle, the work done is [37]:

$$W = \dot{m} \bullet (h_3 - h_4) - \dot{m} \bullet (h_2 - h_1) = \dot{m} \bullet C_p \bullet (T_3 - T_4 - T_2 + T_1) \tag{9}$$

, and the heat added into the system per second is given by:

$$Q_{2,3} = \dot{m} \bullet (h_3 - h_2) = \dot{m} \bullet C_p \bullet (T_3 - T_2) \tag{10}$$

Thus, the engine's thermal efficiency is defined as [38]:

$$\eta = \frac{W}{Q_{2,3}} = 1 - \frac{1}{\pi^{\frac{k-1}{k}}} \tag{11}$$

where π is the pressure ratio in the compressor. In the LEG model, the friction model is fully considered, so the actual engine efficiency needs to deduct the effect of friction.

3.2. Linear generator model

In the simplified 2D model built by Magnet, an axisymmetric magnetic field transient analysis method is utilized. The circuit is of the three-phase coil Y connection type, and the motor itself is a 3-phase, 12-slot/7-pole tubular permanent magnet (PM) motor equipped with modular stator windings where the coils of each phase are arranged consecutively [39]. The electromotive force (EMF) is induced in the stator coils due to the changes in the magnetic flux described by Faraday's law [40]. For the coil of N turns per phase, x as the displacement

and φ as the magnetic flux, the instantaneous induced EMF is expressed in Equation (12) [41]:

$$EMF = -N \bullet \frac{d\varphi}{dt} = -N \bullet \frac{d\varphi}{dx} \bullet \frac{dx}{dt} \tag{12}$$

The circuit of each phase of the permanent magnet synchronous motor includes an EMF source equal to the no-load EMF, fed into series reactance and resistance, R_e [42]. When there is a load $R_{e,E}$, the phase current is expressed in Equation (13) [40]:

$$EMF = V_E + V_L + V_r = I \bullet R_{e,E} + L_i \bullet \frac{dI}{dt} + I \bullet R_{e,r} \tag{13}$$

where V_E is the voltage for the external load $R_{e,E}$, and V_L is the induced voltage, V_r is the voltage of the coil resistance $R_{e,r}$. I is current, L_i is the constant value of inductance, which is calculated with Equation (14):

$$L_i = \frac{\psi_i}{I} \tag{14}$$

where ψ_i is the flux linkage due to current. Besides, the total flux linkage is subdivided into two parts, they are the armature excitation, ψ_i, and the flux around the magnetic circuit driven by the PMs, ψ_{PM}.

The magnetic force ($F_{magnetic}$) is calculated with Equation (15), where $\dot{x}$ is the armature speed [43]:

$$F_{magnetic} = \frac{V_E \bullet I}{\dot{x}} \tag{15}$$

The performance of the LG magnetic force, current, and voltage of single-phase changes, along with the changes in the velocities and positions, are depicted in Fig. 4. In Fig. 4 (a), the magnetic force is depicted with varying positions and velocities of the LG mover. As the position changes from 0 mm to 120 mm and the velocity ranges from 0 m/s to 8 m/s, the magnetic force reaches a peak of 800 N, with negative values appearing when the direction of motion changes. Moreover, Fig. 4 (b & C) describe the changes in current and voltage of single-phase along with
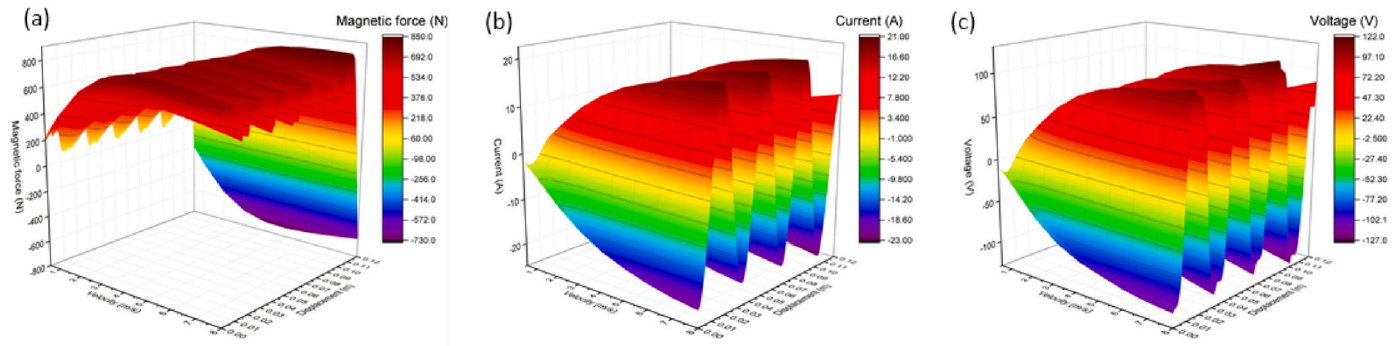
Fig. 4. (a) Magnetic force (b) single-phase current and (c) single-phase voltage of the linear generator versus velocity of the translator and its relative position while the load is 6 Ohm.

different positions and velocities. The current and voltage values are limited to 20 A and 100 V, respectively, and fluctuations are observed as a result of the impact of the coils and magnetic distribution. LG's performance is output in the form of tables and coupled to the linear engine in look-up tables; During the simulation, once the position and velocity of the mover were determined, there would be the determined current, voltage, magnetic force, and power output.

3.3. Model validations and assumptions

The LEG model is to be validated using experimental data from a previous open-loop linear engine testing rig [24], and a standalone linear generator rig [44], before being integrated into a multidisciplinary (both mechanical and electromagnetic) model to predict the performance of the proposed closed-loop systems, which will be elaborated in the sections below. The LEG model introduced in this paper is more than a simple theoretical thermodynamic model, as multiple practical losses in linear engine and linear generator parts have been considered thoroughly in various sub-models introduced in the published papers.

In the previous model of a linear engine [23], gas leakage through double-acting pistons in both the expander and compressor, gas compression/throttling through the intake/exhaust valves, and heat losses through various cylinder heads, liner, and other pipes were considered and reflected in the relevant sub-models. In a more recent paper [24], the friction model of a linear engine was deduced to reflect a multiple graphite piston ring mechanism, and graphite/steel contact surfaces used on the rig, which could accurately predict the measured friction forces (see Fig. 6 of reference [24]). In the recent development of the second generation of LEG testing rig, detailed valve lifting profiles have been measured at different working conditions and used to displace oversimplified on/off valve lifting profiles in the previous versions.

The LEG model uses an LG model with 2D symmetric geometries developed in MagNet software, rather than an ideal 1D equivalent damper model used in the previous LJEG model. In a recent paper [44], a thorough comparison of different topologies of LG to be integrated with linear engines was investigated, which shows a short translator/-long stator tubular type of LG (linear synchronous PM machines) demonstrated the best performance in the experimental study. This LG model had developed from the earlier models in Refs. [39,45], and it showed a good accuracy to predict electromagnetic force, EMF, and the current per phase against the experimental data (see Fig. 13 in Ref. [45], Figure 25 in Ref. [44], and Figure 20 in Ref. [46], respectively). In this study, the same LG model with different dimension data is applied. The LG model displaces the moving mass load in the linear engine model to provide the first multidisciplinary dynamic model of LEG to allow the further accurate prediction of the proposed closed-loop systems.

Lastly, the assumptions of the whole LEG model will be listed and explained in Section 3.3.3.

3.3.1. Linear engine validation

The first-generation of the Joule cycle LEG testing rig, also named Linear Joule Engine generator (LJEG) in a previous paper [24], is used to validate the linear engine mode of the LEG model. The LJEG testing rig equips with a double-acting expander featuring an effective bore of 80 mm, a double-acting compressor with a bore size of 70 mm, a maximum stroke of 120 mm, and a moving mass representing the electromagnetic resistance. In Ref. [23], detailed experimental data were presented, including the measured expander pressure (Figs. 9 and 10 of the reference paper). The LJEG rig was operated at a frequency of 7 Hz and 110 mm stroke. In Fig. 5 (a), (b), and (c), the comparison of experimental and simulation results is presented for piston velocity, acceleration, and displacement within a single cycle. The linear generator model of the LEG model has been displaced with a moving mass sub-model to duplicate the LJEG rig. Maximum errors of three parameters in comparison are 7.28%, 4.73%, and 1.52%, respectively. In terms of these parameters of dynamics, it shows that a high precision could be achieved using the linear engine model while various practical losses have been considered.

3.3.2. LG validation

The first standalone LG testing rig was a long translator/short stator, 3-phase, 6-slot/14-pole type. To match with the linear engine, it was designed with a rated force of 800 N, a maximum stroke of 120 mm, and the moving mass (including the translator and the shaft) was 6 kg in total [39]. The LG model developed in MagNet showed good alignment with the measured data from this rig, which was presented in Fig. 13 of the paper [45]. An electromagnetic force analysis showed that the errors are within 4.74% for the forward cogging force and 4.30% for the backward cogging force respectively.

The second standalone LG testing rig was designed as a short translator/long stator tubular type machine after the design optimization study shown in Ref. [44]. To test the new type of LG's performance, a small rig was built with a stroke of 50 mm, an air gap of 2.5 mm, and a mover mass of 4.4 kg. The experiment and the simulation results of the induced no-load back EMF and the three-phase short circuit currents exhibited satisfactory agreement, as reported in Figures 18 and 20 in reference [46]. The observed results showed a 9 V peak EMF and a 1.69 A peak current, while the simulation yielded approximately a 9.9 V peak EMF and 1.86 A peak current. The experimental discrepancy is primarily attributed to design tolerances in the manufacturing process, such as the magnetic gap size between the stator and translator, as well as the presence of parasitic gaps between stator segments. To this date, a fully validated LG model in MagNet is available, which is used as the basis for new prototype development. The simulated performance of a full-size, short translator/long stator tubular type of LG (linear synchronous PM machine) with 120 mm stroke is presented in Fig. 4.
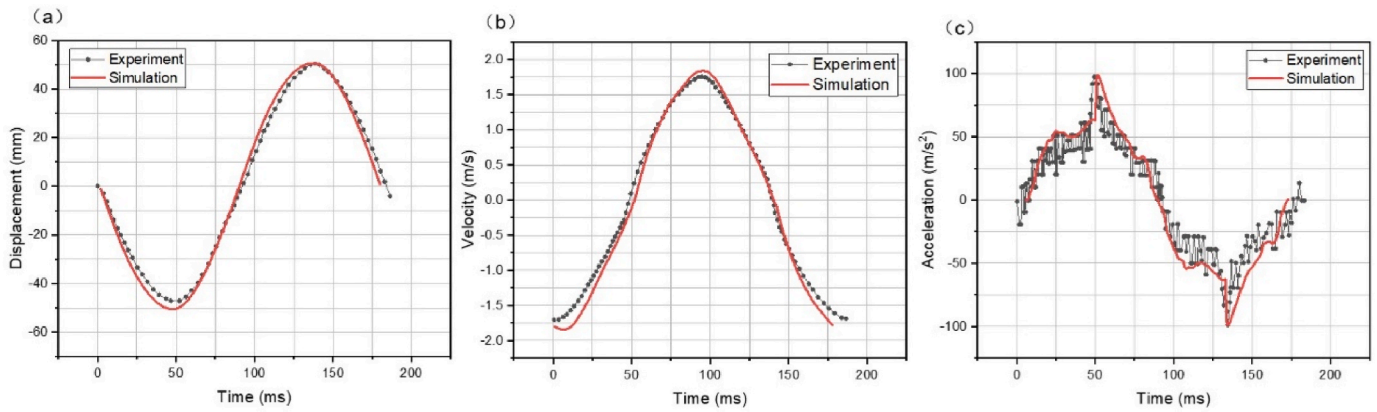
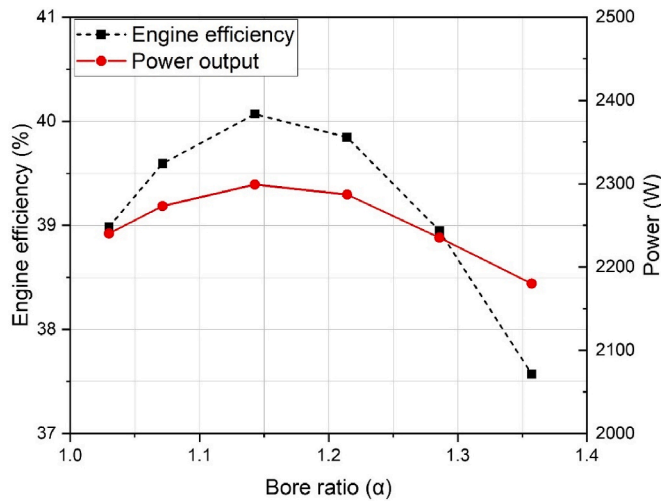**Fig. 5.** Experiment and simulation results of the mover's (a) displacement, (b) velocity, (c) acceleration.

Fig. 6. Power and engine efficiency changes of the open-loop air model with different bore ratios.

3.3.3. Solvers and assumptions

Siemens Simcenter AMESim and MagNet were used to build the linear engine model and LG model, respectively. In MagNet, the LG model is a 2D model, and the motion source type is velocity-driven. The solver iteration method is Newton Raphson Iteration with a tolerance of 0.1%. AMESim uses a set of variable time-step numerical integration solvers, which could autonomously switch between the most efficient methods. The integrator tolerance is $1 \times 10e{-}6$ s. In AMESim, the property libraries of real working fluids and parts materials will have crucial impacts on the accuracy of the LEG model. However, the multidisciplinary model with all real property inputs would require extensive computing time, a detailed investigation on how to reduce computing time and generate credible results has been conducted as follows.

Three different working fluid property models are applicable in the linear engine model, namely Perfect Gas, Semi-Perfect Gas and Real Gas (based on Van Der Waals equation). The simulation results are compared in Table 2, which shows a negligible discrepancy for an open-loop LEG using Semi-Perfect or Real Gas properties. This is due to the air properties demonstrating limited difference apart from those at the low end of the temperature range [47]. However, the gas property model cannot be further reduced to a Perfect Gas assumption which regards a constant heat capacity. To balance the accuracy and the computing resource requirement of the LEG model, a Semi-Perfect gas property model is adopted in the study.

Table 2
The comparison of the LEGs using three types of air definitions.

Properties definition	Unit	Perfect	Semi-perfect	Real (Van der Waals)
Air composition	[−]	0.78109 N_2, 0.20954 O_2, 0.00937 Ar		
Engine efficiency	[%]	37.50	40.07	40.09
Mean mechanical power output	[W]	2152.84	2299.83	2300.76
Max temperature in the compressor	[K]	588.62	661.50	662.64
Max pressure in the compressor	[bar]	16.08	18.35	18.34
Max temperature in the expander	[K]	1056.81	1130.83	1129.26
Max pressure in the expander	[bar]	15.44	17.67	17.68

Therefore, for the closed-loop LEG model, the properties of the working fluids, i.e., air, argon, and helium at standard temperature and pressure (STP) are listed in Table 3 [47]. To keep consistency, Semi-Perfect gas property models are used for performance prediction.

3.4. Energy analysis and exergy analysis

Energy flows in multiple directions in LEG, and the process studied focused on the main components of the compressor, HTHE, expanders, LG, and condenser for the closed-loop LEG. Within the whole cycle, the energy balance is described by Equation (16) [48], where E_{heater} is the energy input from the heat exchanger. $E_{exhaust}$ is the energy of the exhaust gas, and E_{intake} is the energy of the intake gas. $Q_{dissapation}$ is the heat dissipation to the ambient, $P_{Friction}$ is the negative work from friction, W is the mechanical power output.

$$E_{heater} = (E_{exhaust} - E_{intake}) + Q_{dissapation} + P_{Friction} + W \qquad (16)$$

Exergy represents the maximum useful work that a system can produce. Its value can be impacted by the surrounding environment [49].

Table 3
The properties of the working fluids for closed-loop LEGs.

Properties at STP	Unit	Air	Argon	Helium
Density, ρ	[kg/m^3]	1.18	1.63	0.16
Molar mass, M	[g/mol]	28.97	39.95	4.00
Specific heat ratio, k	[−]	1.40	1.67	1.67
Heat capacity at constant pressure, C_p	[J/(kg • K)]	1004.73	520.33	5193.18
Absolute viscosity, v_g	[cP •10^{-3}]	18.46	22.61	19.84
Thermal conductivity, k_g	[W/(m • K) •10^{-3}]	26.03	17.70	155.06

The analysis of exergy destruction helps identify the primary contributors to the process's irreversibility [49]. The exergy destruction $E_{x,i}$ is calculated from Equation (17) and the enthalpy exergy is calculated from Equation (18) [50]:

$$E_{x,i} = E_{x,Q,in} + E_{x,H,in} - E_{x,H,out} - E_{x,Q,out} - W \tag{17}$$

$$E_{x,H} = (H - H_0) - T_0(S - S_0) \tag{18}$$

where $E_{x,H}$ is the enthalpy exergy of the intake (subscript is *in*) and exhaust (subscript is *out*) working fluid. $E_{x,Q}$ is the thermal exergy related to the intake of heat or heat dissipation. H is the enthalpy and S is the entropy, the subscript *0* refers to the ambient conditions: 293.15 K and 1 bar. The thermal exergy related to the heat transfer Q is expressed in Equation (19) [51]:

$$E_{x,Q} = \left(1 - \frac{T_0}{T}\right) \bullet Q = k_{th} \bullet S_{th} \bullet \left(T + \frac{T_0}{T} - 2 \bullet T_0\right) \tag{19}$$

In this case, the exergy destruction in the compressor, HTHE, expander, and condenser are expressed in Equations (20)–(23), respectively [52]:

$$E_{x,compressor} = E_{x,H,in} - E_{x,H,out} - E_{x,Q,out} + W_{compressor} \tag{20}$$

$$E_{x,HTHE} = E_{x,H,1,in} - E_{x,H,1,out} + E_{x,H,2,in} - E_{x,H,2,out} \tag{21}$$

$$E_{x,Expander} = E_{x,H,in} - E_{x,H,out} - E_{x,Q,out} - W_{Expander} \tag{22}$$

$$E_{x,Condenser} = E_{x,H,1,in} - E_{x,H,1,out} + E_{x,H,2,in} - E_{x,H,2,out} \tag{23}$$

where subscripts 1 and 2 mean the hot side and cold side, and the subscribe *in* and *out* represent the inlet and outlet. Based on reference [53], the exergy destruction in the heat exchanger could also be written as Equation (24), which implies that the temperatures would affect the exergy destruction impressively.

$$E_{x,heater} = \dot{C}_1 \bullet T_0 \bullet \left[\ln\left(\frac{T_{1,out}}{T_{1,in}}\right) + \frac{\dot{C}_2}{\dot{C}_1} \bullet \ln\left(\frac{T_{2,out}}{T_{2,in}}\right)\right] \tag{24}$$

where $\dot{C}$ is the heat capacity rate, and it could be expressed as $\dot{C} = \dot{m} \bullet C_p$.

As for the exergy efficiency (η_x), it is defined as the ratio of the output exergy and input exergy, and the equations of the main components in the LEG are expressed below; however, because the operating temperature of the condenser across the reference temperature, its exergy efficiency could be expresses by Equation (28) [54]:

$$\eta_{x,Compressor} = \frac{E_{x,out} - E_{x,in}}{W_{compressor}} \tag{25}$$

$$\eta_{x,HTHE} = \frac{E_{x,2,in} - E_{x,2,out}}{E_{x,1,in} - E_{x,1,out}} \tag{26}$$

$$\eta_{x,Expander} = \frac{W_{Expander}}{E_{x,in} - E_{x,out}} \tag{27}$$

$$\eta_{x,Condenser} = \frac{E_{x,1,out}^T + E_{x,2,out}^T}{E_{x,2,out}^T + \left(E_{x,2,in}^P - E_{x,2,out}^P\right) + E_{x,1,in}^T + \left(E_{x,1,in}^P - E_{x,1,out}^P\right)} \tag{28}$$

where the E_x^T and E_x^P are the thermal exergy and mechanical exergy.

4. Results and discussions

4.1. Impacts of engine geometries

The ratio of expander bore diameter and compressor bore diameter ($\alpha = D_{b,expander}/D_{b,compresor}$) is evaluated to find the sensitivity to efficiency and power output. The LEG requires proper sizing of the compressor and expander geometry to match the coupled LG, as different LG sizes and performance levels result in different force balances within the LEG system [19]. This, in turn, results in varying optimal bore diameter ratios for maximum power output and engine efficiency [25]. Considering the LEG performance and the design requirements, the compressor bore diameter of 70 mm is selected for the prototype and models. Fig. 6 shows that the ratio to achieve optimal power and engine efficiency is around 1.17.

As the bore ratio increases, both the force exerted by the expander gas and the friction increase, leading to an increase in velocity and magnetic force. However, as the effect of the increased expander gas force is offset by the increased friction gradually, there is an initial increase followed by a decrease in mechanical power output. The engine efficiency is impacted by energy input and power output. With ratio increases, the mass flow rate increases from 11.37 g/s to 12.48 g/s, but with a decreasing increase rate. Limited by a peak temperature of below 1095 K, the input energy must change with the mass flow, causing slight change differences in engine efficiency and power output.

4.2. Impact analysis of inert gas working fluids

Four simulation cases were carried out and compared in Table 4: the air standard open-loop, and closed-loop versions using air, helium, and argon as the working fluids. When the intake pressure and temperature are 0.85 bar and 225 K, the closed-loop air system has the highest power output of 2448.22 W, followed by the open-loop air system with 2299.83 W. Meanwhile, the closed-loop argon (Ar) system has the smallest power output of 1850.39 W. However, the closed-loop helium (He) system has the highest engine efficiency of about 51.30%, while the open-loop air system has the lowest engine efficiency of about 40.07%.

Between the air systems, the closed-loop configuration performs better in terms of power output and engine efficiency. This is due to the

Table 4
The settings and the performances of the open-loop and closed-loop models.

Model types	unit	Open-loop	Closed-loop	Closed-loop	Closed-loop
Working fluid	[–]	Air	Air	Argon	Helium
Total input power	[W]	5740.00	5574.00	4230.00	3986.00
Engine efficiency	[%]	40.07	43.92	43.74	51.30
Mean mechanical power output	[W]	2299.83	2448.22	1850.39	2044.66
Mean electricity power output	[W]	2000.35	2116.62	1624.58	1788.64
Generator efficiency	[%]	86.98	86.46	87.80	87.48
System efficiency	[%]	34.84	37.98	38.41	44.88
Operation frequency	[Hz]	15.5	16.5	13	14
Piston amplitude	[mm]	116.68	116.80	116.48	116.55
Peak piston velocity	[m/s]	5.06	5.11	4.55	4.83
Compressor intake pressure	[bar]	1	0.85	0.85	0.85
Compressor intake temperature	[K]	293.15	225	225	225
Peak temperature of the compressor	[K]	661.50	612.5	626.80	673.80
Peak temperature before the expander	[K]	1093.15	1091.50	1091.03	1090.91
Peak temperature of the expander	[K]	1130.83	1177.68	1047.46	1074.41
Peak pressure in the compressor	[bar]	18.35	23.76	10.87	13.18
Peak pressure in the expander	[bar]	17.67	22.99	10.31	12.62
Compressor chamber peak volume	[cm^3]	448.95	449.57	448.39	448.21
Expander chamber peak volume	[cm^3]	616.11	616.34	615.21	615.54
Mean mass flow rate	[g/s]	12.05	10.90	18.19	1.89

higher pressure and temperature achieved at the compressor discharge in the closed-loop case, as observed in Figs. 9 and 10. Among the closed-loop systems, the air system shows advantages in terms of power output, while the He system boasts the best engine efficiency. The differences in performance between the closed-loop systems can be attributed to the thermophysical characteristics of the working fluids [25], as shown in Table 3; and based on Equation (11), the thermal engine efficiency is a function of the pressure ratio (π) [55] and specific heat ratios [38]. Therefore, the difference in these parameters results in the engine efficiency variation, aligning with the results by calculating the ratio of mechanical work output to heat input.

The closed-loop He system has the lowest mass flow rate of 1.89 g/s, the closed-loop Ar system has the largest of 18.19 g/s, and the air system does not show an advantage in it. However, the total energy input is the product of the mass flow rate, temperature changes, and heat capacity, so the air case has a larger input power of above 5500 W. In contrast, the argon and helium cases have input power below 4500 W. Furthermore, the mean power output level is affected primarily by the velocity, reflected by the frequencies. While the temperatures before the expanders remain below 1095 K in all cases, the transient temperature in the expander for air systems is higher, which results from recompression, the air-spring activity of the remaining working fluid until the expander inlet valve opens.

Fig. 7 (a) represents the changes of the forces during one cycle for the open-loop air system, which reflects the forces changes in the closed-loop systems to some extent. The expander peak force approaches 9000 N and is larger than the compressor peak force, where the pressure in the chambers and the cross-section area of the pistons determine the forces. The magnetic force fluctuation reflects the distributions of the coils and magnets described in Ref. [19]. The motion dynamics of the four cases are described in Fig. 7 (b). The closed-loop air system exhibits the highest peak velocity of 5.11 m/s, while the closed-loop Ar system has the least peak velocity of 4.55 m/s. The piston dynamics are influenced by the valve timing, load, and pressure. While the stroke is fixed, peak pressure varies, and the rankings of velocity and acceleration are the same as the ranking of the peak pressures.

The mass variation of the working fluid in the chambers could reflect the working process of the LEG in detail. Fig. 8 displays the mass changes in the right-hand compressor and left-hand expander as a function of piston displacement, corresponding with the cases in Table 4. In line AB, Fig. 8 (a), the compressor inlet and exhaust valves are closed, BC is the compressor fluid inlet, CD is the compression process, and the exhaust valves open through DA until the operation bottom dead center (OBDC). In line EF, Fig. 8 (b), the expander exhaust valve closes, and fluid recompression occurs until the operation top dead center (OTDC). FG is the expander inlet, and GH is the expansion process. Line HIE is the exhaust phase, while HI represents the sudden change in piston direction

and a sudden decrease in working fluid mass, IE shows a gradual decrease in the mass. Moreover, the open-loop air system requires more mass than the closed-loop air system due to differences in compressor intake pressure and temperature, which impact the pressures and densities in the chamber. With Ar as the working fluid, the peak mass is about 0.84 g, while He is about 0.084 g. The air spring causes the peak mass difference between the compressor and expander, while the mass transfer between the compressor and expander remains the same.

Fig. 9 shows the changes in the pressure and volume of the working fluids, and Fig. 10 shows the changes in the temperature and specific entropy. The Joule cycle LEG comprises five main processes: compressor suction, compression, heating, expansion, and exhaust, as described by the arrows in Fig. 9. The compression ratio (CR) is limited by the real OBDC, point D (Fig. 8 (a)), and the positions of point D in four cases could reflect the peak pressure ranking to some extent.

The different peak pressures are related to the heat inputs and the thermal properties of the working fluids. During compression, based on Equation (6) and Equation (7), the pressure could be expressed as $P = constant \bullet T^{\frac{k-1}{k}}$. The specific heat ratio difference leads to higher peak pressures for air compared to helium and argon [56]; and the different start-up states of the air cases result in the highest peak pressure being achieved in the closed-loop air case, followed by the open-loop air case. Argon requires more heat exchanger energy than helium due to differences in density and heat capacity at constant pressure. The lower thermal conductivity of argon also results in a longer heating time, leading to a lower frequency and lower pressure in the argon system. This results in the compressor exhaust valve opening earlier and lower peak pressure in the argon system.

In Fig. 10, the specific entropies in the compressors and expanders are nearly constant, with minor changes. Under the ideal Joule cycle, the entropy should remain the same during the compression and expansion. However, intake and exhaust processes cause entropies fluctuation; the heat dissipation occurs mainly around OBDC, which also accounts for the fluctuation. Fig. 10 also reflects the chamber temperature changes; closed-loop cases have the same intake temperature, lower than the open-loop air case. The closed-loop He case has the compressor's highest temperature of 673.80 K, and the air system has the lowest temperature of 612.5 K. In the expanders, the closed-loop air system exhibits the highest temperature of 1177.68 K, followed by the open-loop air version, closed-loop He version, and closed-loop Ar version, which corresponds to the peak pressure ranking.

Apart from the comparison of the air cases above, the effects of the inlet pressure and temperature on the LEG performance are shown in Fig. 11. Three inlet states were evaluated for the closed-loop versions of the working fluids (air, argon, and helium). The results showed that lower inlet pressure and temperature improve engine efficiency. At low temperatures, and 0.78, 0.87, and 0.85 bar for air, argon, and helium,
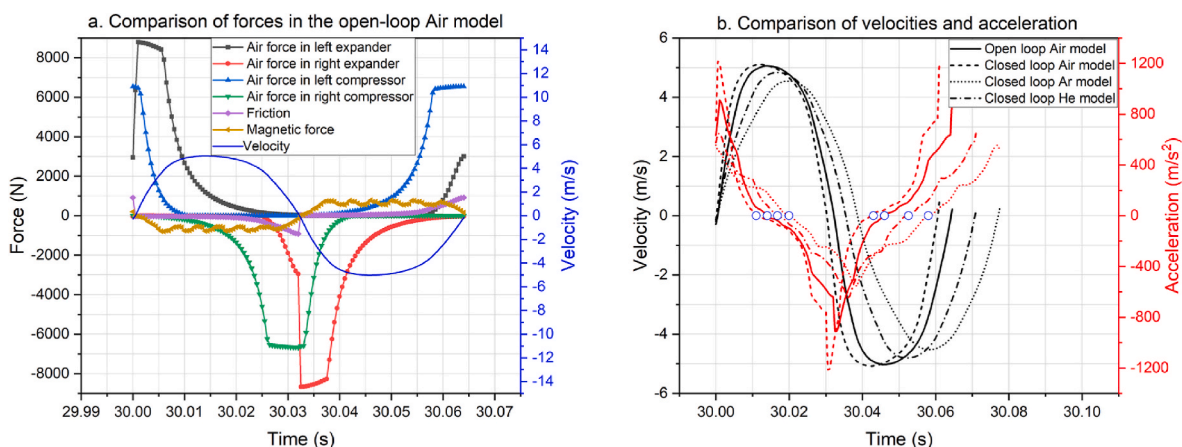

Fig. 7. Comparison of the (a) forces, and (b) velocities and accelerations of the LEG.
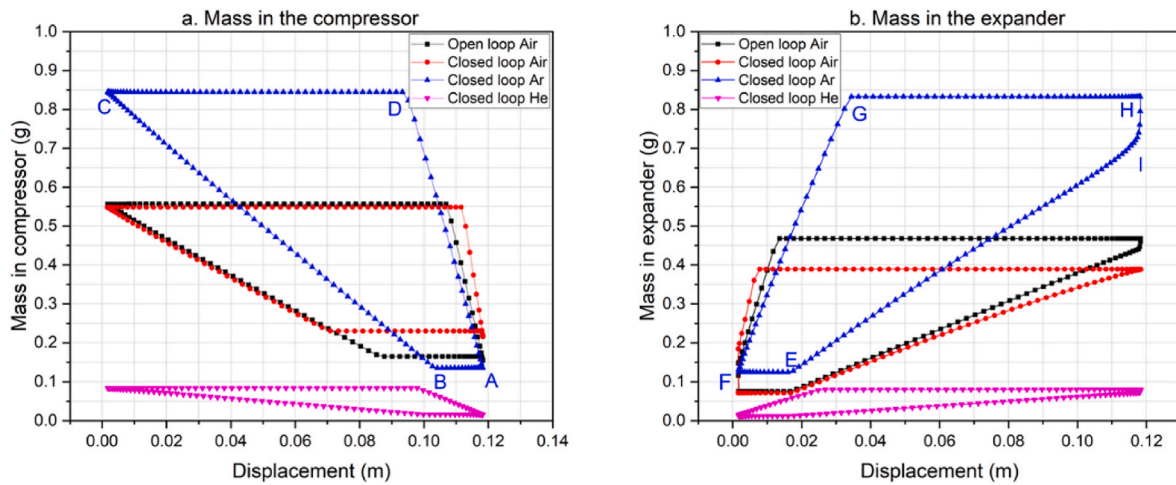
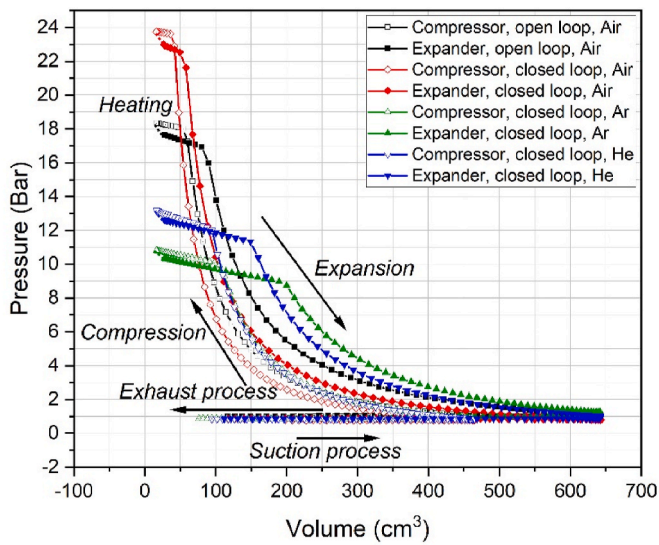**Fig. 8.** Mass changes in (a) compressor and (b) expander.
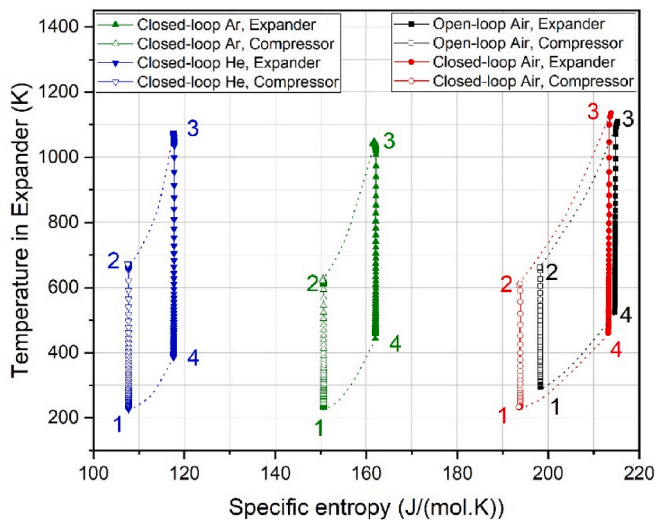

Fig. 9. Pressure versus volume.

Fig. 10. Temperature versus specific entropy.

the theoretical engine efficiencies were 45.06%, 43.77%, and 51.30%, respectively; these represent about 13%, 44%, and 34% improved efficiency than ambient conditions. Proper control of valve timing can improve CR, thereby improving engine performance; adjusting the inlet pressure and temperature is an effective way to achieve this. Therefore, the closed-loop configuration shows merits in achieving better performance.

4.3. Engine performance maps

The LEG performances of the models are summarized in Figs. 12 and 13, which describe the magnitude and variation tendency of the engine performance characteristics. Overall, each type of map is similar, especially the power map. An increase in frequency and Break Mean Effective Pressure (BMEP) results in a corresponding increase in power output, but the highest engine efficiency is achieved at a moderate frequency and high BEMP. The peak BMEP value is observed to be around 2.47 bar, which is lower than the BMEP of up to 20 bar for gasoline engines [57] and over 30 bar for diesel engines [58], but comparable to two-stroke engines utilized in hand-held power tools [59]. This relatively low level of BMEP is attributed to the short intake duration of the expander, which reduces the volumetric heat value [60], and the low peak pressure [61]. The port/valve timing determined the duration of the expander inlet, and Fig. 9 describes the sharply decreasing pressure in the cylinders and low level of mean in-cylinder pressure, which reflect the low-level BMEP directly.

In detail, Fig. 12 depicts the engine efficiency maps, where the closed-loop He system has the largest peak engine efficiency of about 56.27%, followed by the Ar system. Air versions have lower levels of peak engine efficiencies, and the open-loop air version has the smallest peak engine efficiency of 40.85%. Fig. 13 depicts the power changes as a function of frequency and BMEP, with the closed-loop Ar system recording the highest peak power of 3610 W, followed by a closed-loop He system at 3560 W. The higher CR leads to higher peak engine efficiency of 44.19% in the closed-loop air system than the open-loop version [55], but the lower mass flow rate limits the peak power output to be the smallest of 2775 W; while a higher mass flow rate leads to a higher power output of the open-loop system reaching 3040 W. Both the Ar and He closed-loop systems could achieve higher maximum-output-powers than the air versions due to their accessible higher frequencies, which also results in increased mass flows and higher CRs. Peak efficiency and power output operate at different frequencies and BMEP; however, based on the performance maps, the appropriate frequency and BMEP can be selected to obtain desired efficiency and power simultaneously.
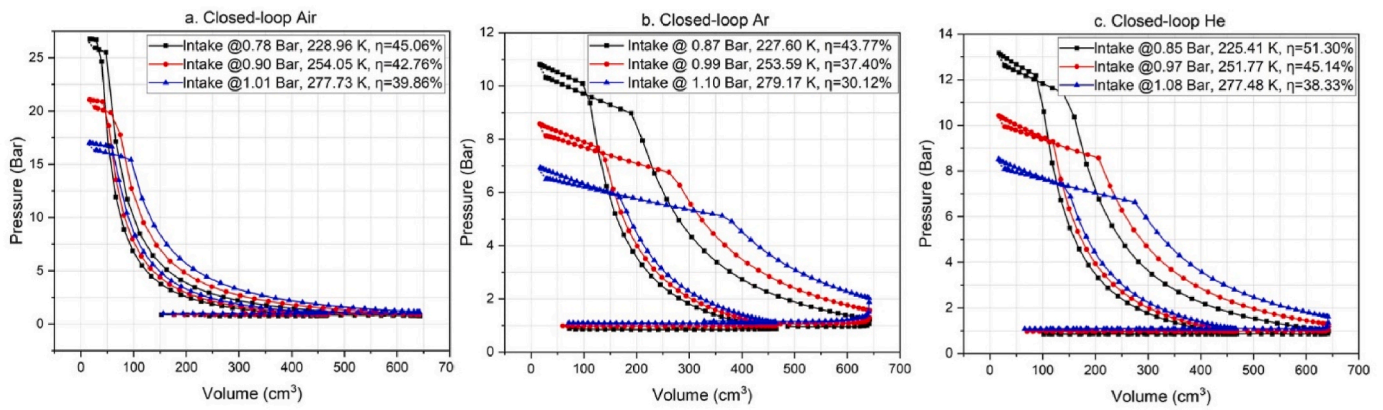
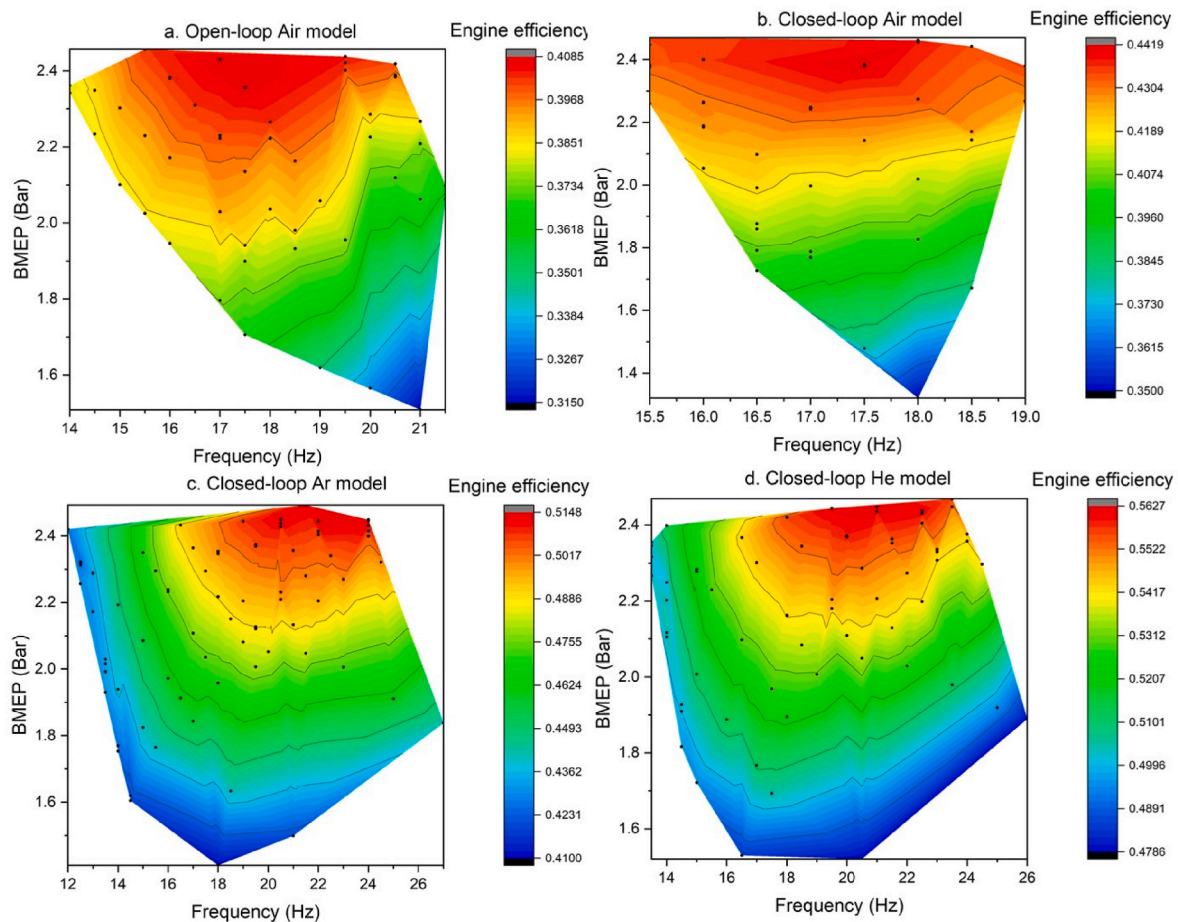**Fig. 11.** The effects of the intake states of the working fluids, (a) air, (b) argon, and (c) helium.

Fig. 12. Engine efficiency of four cases.

4.4. Energy and exergy analysis

During one complete cycle, heat energy is extracted through the HTHE, and flows in several directions, including heat dissipation, mechanical power output, friction loss, and exhaust energy loss, including direct discharge or through a condenser.

The energy analysis was carried out based on the cases presented in Table 4. The distributions and the proportions of the energy are presented in Fig. 14. The closed-loop He system produces the highest mechanical power output proportion/efficiency of 51.30%, while the open-loop air system has the lowest, 40.06%. The exhaust energy loss process

is described in Fig. 10, from point 4 to point 1. The proportion of the He version is the least, 35.43%, which is lower than the efficiency; for the open-loop and closed-loop air systems, the proportions of the exhaust energy losses are larger than the argon and helium systems, and larger than their efficiencies.

Friction loss accounts for between 7.40% and 9.30%, mainly affected by the chamber pressures, velocity, and total input energy. Of the various components of frictional power, the frictional power caused by pressure loads contributes the most, based on the friction model validated in Ref. [24]. The pressure in the chamber and the velocity are therefore the most important factors affecting the frictional power.
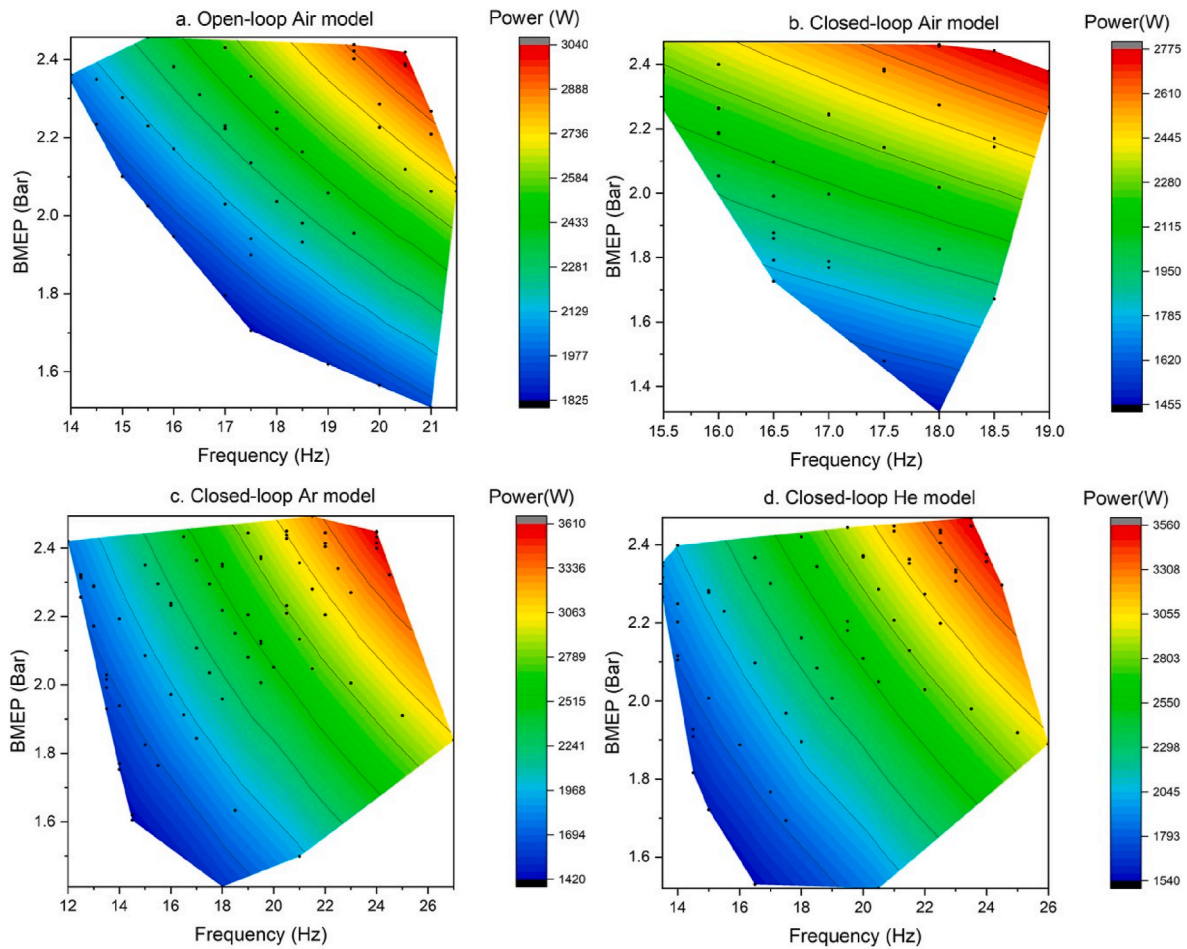
Fig. 13. Engine power output of four cases.

The compressor pressures in the air cases are higher than in the closed-loop Ar and He systems, and the velocities of the air cases are higher, which leads to higher friction power in open-loop and closed-loop air cases. However, the friction peak does not occur synchronously as the peak velocity and its value varies based on the force balance, resulting in a closed-loop air system with less friction power loss than the open-loop air system. Therefore, taking into account the differences in energy input and frictional power loss, the order of friction loss proportions is the highest for the closed-loop He version, second highest for the closed-loop Ar version, and lowest for the closed-loop Air version. The energy lost through heat dissipation mainly happened in compressor and expanders, and accounts for 2.95%–4.37%, due to temperature differences and total input energies.

In conclusion, the exhaust losses are comparable to the mechanical power output in all cases, and can be recovered, stored, or used directly in cogeneration to improve system performance. Modifying the design and material choices of the piston ring can also reduce friction loss and improve system efficiency.

Exergy destruction refers to the loss of useful energy resulting from irreversible processes such as mixing the different states of working fluids, heat transfer, and frictional effects [62]. The exergy analysis was carried out on the main 4 components of the LEG model, including the compressor, HTHE, expander, and possibly condenser.

Fig. 15 displays the exergy destruction rates (i) for all the main components in the four cases. The compressors and expanders have low exergy destruction rates, all below 200 W, while the condensers have the largest one, followed by the HTHEs. Based on Equation (24), the most important factors are the inlet and outlet states of the hot and cold sides. Affected by the temperature difference, exergy destruction rates in the

condensers were larger than in the HTHEs, where the cold side and hot side temperature ratios are comparatively smaller. The smallest temperature changes of the hot side and cold side through the HTHE and the small heat capacity rate lead to the lowest exergy destruction rate in the closed-loop He system, while the closed-loop argon system has the largest value among the four systems, 500 W; the smallest temperature changes of the hot side and cold side through the condenser also leads to the lowest exergy destruction rate of 376 W in the helium system, while the closed-loop Air system has the largest exergy destruction rate of 1384 W. In terms of the proportion of exergy destruction, the condenser occupies an absolute proportion, 69.51%, 57.96%, and 61.79% for the air, argon, and helium cases, due to the difference in the inlet and outlet states. The HTHE accounts for about 19.19%–62.83%, while it ranges from 2.21% to 11.52% for the expander, and the larger data come from the open-loop air case. Therefore, the expander has minimal effects on the exergy destruction structure of the system, and the condenser is the highest priority of optimization, followed by the HTHE.

The exergy efficiencies of the components are compared in Fig. 16, where the exergy efficiencies in compressors and expanders are similar, larger than 96%, which are in line with the reported efficiencies of compressors and turbines in Joule cycle gas turbines, as summarized in Ref. [63]. The exergy efficiencies in the HTHE are around 90%, but the exergy efficiencies of condensers are below 18%. The low level of the exergy efficiency of the condenser results from the coolant's low temperature [64], which is below the reference temperature, and the condenser's exergy efficiencies correspond with the largest exergy destructions.
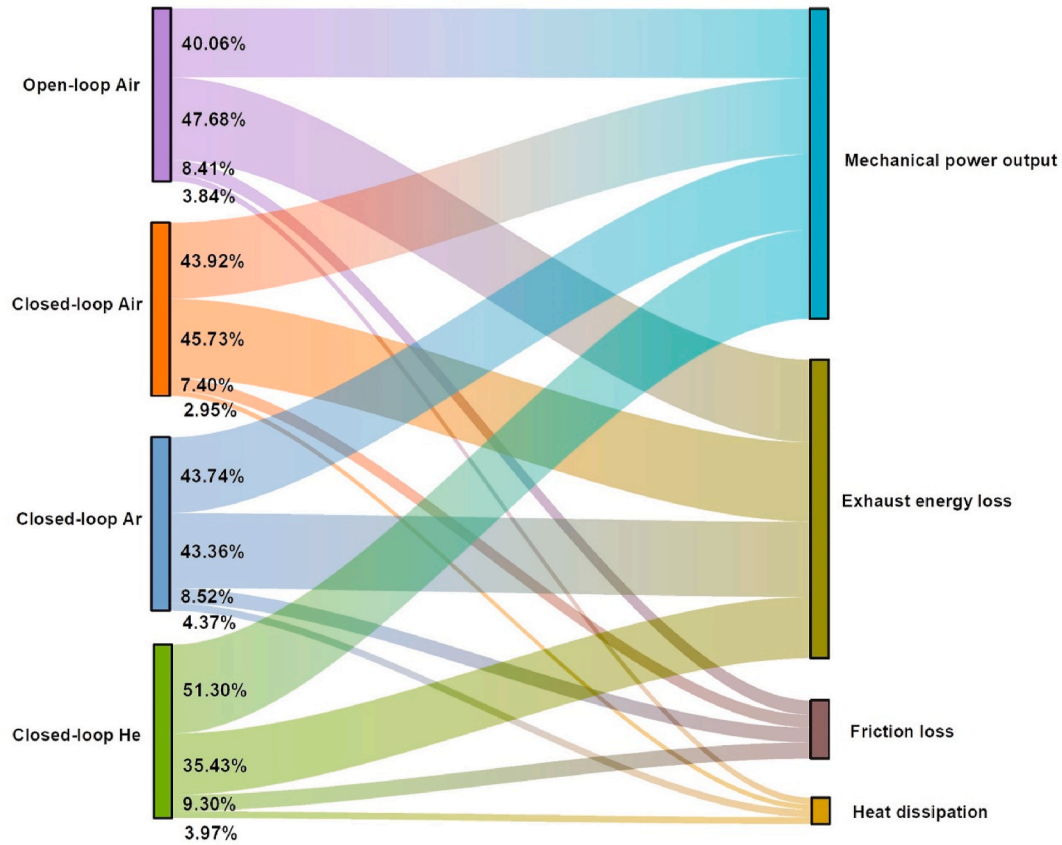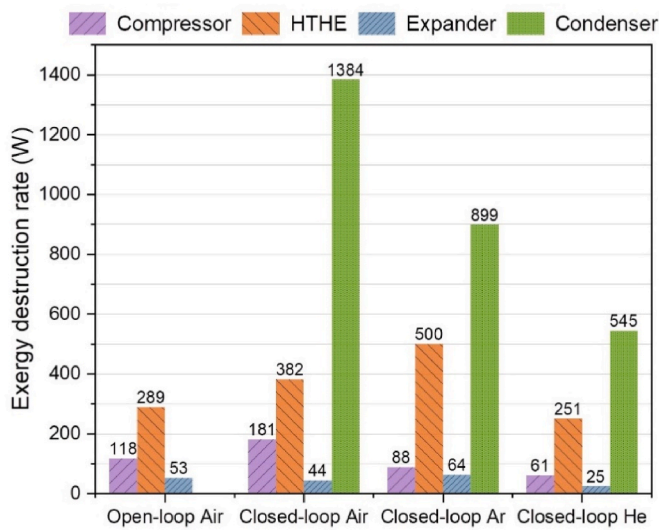
Fig. 14. Comparison of the energy flow.

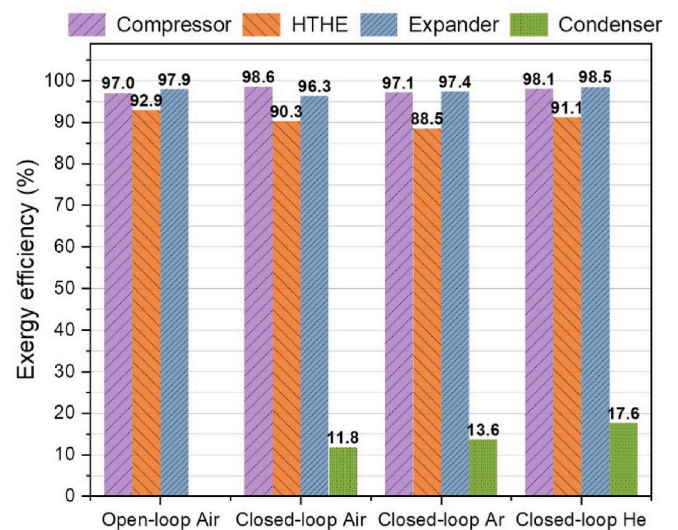**Fig. 15.** Exergy destruction rates in the components of the four cases.

Fig. 16. Exergy efficiency of the components of the four cases.

5. Conclusion

The performance prediction and energy analysis of a proposed closed-loop LEG concept have been presented in the paper, which is based on a validated open-loop LEG model. Air, argon, and helium were used as working fluids and compared comprehensively in this study. The main conclusions are as follows.

(1) The linear generator and linear engine should be matched to attain desired integrated performance. The expander and compressor geometric ratio influences engine performance.

(2) Keeping the low-pressure side of the closed-loop LEG sub-atmospheric benefited engine performance because of the influence on the achievable pressure ratio. It led to improved efficiency of 44% for the argon version and 34% for the helium version.

(3) The closed-loop cycle helps improve LEG's performance because of the flexibility and controllability of heat removal at the heat sink side of the cycle. With air as the working fluid, its efficiency could reach 43.92% in the closed-loop version compared to the maximum of 40.07% in an optimal open-loop version; also, the mechanical power output increases by about 6.45% in the closed-loop version.

(4) For the closed-loop system, when Helium is used, it achieved the highest engine efficiency of 51.30%, compared to the peak efficiency of 43.74% achieved using Argon as the working fluid. The specific heat capacity at constant pressure and the working fluid mass flow rate in the system influence LEG's power output. The specific heat ratio of the working fluids also poses a significant impact on peak pressure, in turn, thermal efficiency and power output.

(5) The optimal engine efficiencies and power output cannot be achieved under the same conditions simultaneously according to the LEG engine map. The restriction of longer valve timings and the steep pressure drop profile in the cylinder limited LEG's BMEP compared to conventional internal combustion engines. The exhaust energy loss accounts for the largest fraction of the losses in a LEG.

(6) The exergy destruction rates within the compressor and expander are relatively low, while the exergy destruction within the condenser ranks first among all components in a closed-loop system. Besides, the exergy efficiencies in the compressors and expanders are above 96% while the exergy efficiencies in condensers are below 18%, which is associated withthe low temperature at the heat sink.

The close-loop LEG design and its promising performance (high efficiency at a relatively low peak temperature of the cycle) demonstrates a potential application occasion where cryogenic liquid fuel evaporation (such as liquified hydrogen) provides sufficient cooling energy at the heat sink and creates a relatively large temperature difference for optimal efficiency of the cycle. Since the interaction between the mechanical part (linear engine) and the electromagnetic part (linear machine) has been revealed using the integrated LEG model, further research focus will be shifted to improving critical components which would greatly affect the key performance indicators of LEG. For instance, the valve and actuation designs improve the thermal efficiency of the linear engine, as well as the overall topology design and material selection of the linear generator, which is the foremost important aspect to increase the overall power density of LEG for commercial applications.

Credit author statement

Mingqiang Li - Writing – original draft, Writing – review & editing, Investigation, Formal analysis. Ugochukwu Ngwaka - Writing – review & editing, Investigation, Validation. Ramin Moeini Korbekandi - Writing – review & editing, Investigation, Validation. Nick Baker – Supervision, Methodology, Conceptualization. Dawei Wu – Supervision, Funding acquisition, Conceptualization. Athanasios Tsolakis – Supervision, Funding acquisition.

Declaration of competing interest

The authors affirm that they do not have any known financial interests or personal relationships that may have influenced the work reported in this paper.

Data availability

Data will be made available on request.

References

[1] Cevik S. Climate change and energy security: the dilemma or opportunity of the century?. 2022.

[2] Joshi A. Review of vehicle engine efficiency and emissions. SAE International Journal of Advances and Current Practices in Mobility 2020;2(5):2479–507.

[3] Hachem H, Gheith R, Aloui F, Nasralla SB. Technological challenges and optimization efforts of the Stirling machine: a review. Energy Convers Manag 2018; 171:1365–87.

[4] Olumayegun O, Wang M, Kelsall G. Closed-cycle gas turbine for power generation: a state-of-the-art review. Fuel 2016;180:694–717.

[5] Ela AMAE, Eldrainy YA, Elkasaby MM, Nour AM. Effect of replacing nitrogen with helium on a closed cycle diesel engine performance. Alex Eng J 2016;55(3): 2251–6.

[6] Zhu S, Yu G, Liang K, Dai W, Luo E. A review of Stirling-engine-based combined heat and power technology. Appl Energy 2021;294:116965.

[7] Kongtragool B, Wongwises S. A review of solar-powered Stirling engines and low temperature differential Stirling engines. Renew Sustain Energy Rev 2003;7(2): 131–54.

[8] Ahmadi MH, Ahmadi MA, Mehrpooya M. Investigation of the effect of design parameters on power output and thermal efficiency of a Stirling engine by thermodynamic analysis. Int J Low Carbon Technol 2016;11(2):141–56.

[9] Zare S, Tavakolpour-Saleh A. Free piston Stirling engines: a review. Int J Energy Res 2020;44(7):5039–70.

[10] Karabulut H. Dynamic analysis of a free piston Stirling engine working with closed and open thermodynamic cycles. Renew Energy 2011;36(6):1704–9.

[11] Cengiz MS, Memis MS, Kaynakli M. The temperature-pressure-frequency relationship between electrical power generating in stirling engines. Int J Eng Res Dev 2017;9(2):59–64.

[12] Ngwaka U, Chen F, Qiu S, Li M, Zhang C, Wu D. Recent progress on performance and control of linear engine generator. Int J Engine Res 2022: 14680874221118014.

[13] Mikalsen R, Roskilly AP. A review of free-piston engine history and applications. Appl Therm Eng 2007;27(14):2339–52.

[14] Kerdchang P, MaungWin M, Teekasap S, Hirunlabh J, Khedari J, Zeghmati B. Development of a new solar thermal engine system for circulating water for aeration. Sol Energy 2005;78(4):518–27.

[15] Udeh GT, Michailos S, Ingham D, Hughes KJ, Ma L, Pourkashanian M. A techno-enviro-economic assessment of a biomass fuelled micro-CCHP driven by a hybrid Stirling and ORC engine. Energy Convers Manag 2021;227:113601.

[16] Ngwaka U, Smallbone A, Jia B, Lawrence C, Towell B, Roy S, et al. Evaluation of performance characteristics of a novel hydrogen-fuelled free-piston engine generator. Int J Hydrogen Energy 2021;46(66):33314–24.

[17] Zhang F, Chen G, Wu D, Li T, Zhang Z, Wang N. Characteristics of ammonia/hydrogen premixed combustion in a novel Linear Engine Generator. Multidisciplinary Digital Publishing Institute Proceedings 2020;58(1):2.

[18] Mikalsen R, Roskilly AP. The free-piston reciprocating Joule Cycle engine: a new approach to efficient domestic CHP generation. China: ICAE 2012. Suzhou; 2012.

[19] Li M, Ngwaka U, Wu D, Zhang F, chen G. The design and simulation of the linear engine generator used for electric propulsion system of the marine transportation and offshore gas/oil platforms. 7th International Conference on Ship and Offshore Technology ICSOT. Indonesia: Surabaya; 2021.

[20] Blarigan PV, Paradiso N, Goldsborough S. Homogeneous charge compression ignition with a free piston: a new approach to ideal Otto cycle performance. SAE Technical Paper 1998:982484.

[21] Clark N, Nandkumar S, Atkinson C, Atkinson R, McDaniel T, Petreanu S, et al. Operation of a smallbore two-stroke linear engine. Proc. of the Fall Technical Conference of the ASME Internal Combustion Engine Division 1998;31:33–40.

[22] Jia B, Zuo Z, Tian G, Feng H, Roskilly AP. Development and validation of a free-piston engine generator numerical model. Energy Convers Manag 2015;91:333–41.

[23] Jia B, Wu D, Smallbone A, Lawrence C, Roskilly AP. Design, modelling and validation of a linear Joule Engine generator designed for renewable energy sources. Energy Convers Manag 2018;165:25–34.

[24] Ngwaka U, Jia B, Lawrence C, Wu D, Smallbone A, Roskilly AP. The characteristics of a Linear Joule Engine Generator operating on a dry friction principle. Appl Energy 2019;237:49–59.

[25] Ngwaka U, Wu D, Happian-Smith J, Jia B, Smallbone A, Diyoke C, et al. Parametric analysis of a semi-closed-loop linear joule engine generator using argon and oxy-hydrogen combustion. Energy 2021;217:119357.

[26] Valenti G, Campanari S, Silva P, Fergnani N, Ravidà A, Marcoberardino GD, et al. Modeling and testing of a micro-cogeneration Stirling engine under diverse conditions of the working fluid. Energy Proc 2014;61:484–7.

[27] Dong S, Shen G, Xu M, Zhang S, An L. The effect of working fluid on the performance of a large-scale thermoacoustic Stirling engine. Energy 2019;181: 378–86.

[28] Chahartaghi M, Sheykhi M. Energy, environmental and economic evaluations of a CCHP system driven by Stirling engine with helium and hydrogen as working gases. Energy 2019;174:1251–66.

[29] Erol D, Calıskan S. The examination of performance characteristics of a beta-type Stirling engine with a rhombic mechanism: the influence of various working fluids and displacer piston materials. Int J Energy Res 2021;45(9):13726–47.

[30] Snarheim D, Imsland L, Foss BA, Ulfsnes R, Bolland O. Control design for gas turbine cycle with CO2 capture capabilities. 2006. p. 57–66.

[31] Sarkar J. Second law analysis of supercritical CO2 recompression Brayton cycle. Energy 2009;34(9):1172–8.

[32] Haunstetter J, Dreißigacker V, Zunft S. Ceramic high temperature plate fin heat exchanger: experimental investigation under high temperatures and pressures. Appl Therm Eng 2019;151:364–72.

[33] Wajs J, Kura T, Mikielewicz D, Fornalik-Wajs E, Mikielewicz J. Numerical analysis of high temperature minichannel heat exchanger for recuperative microturbine system. Energy 2022;238:121683.

[34] Bade M, Clark NN, Musho T, Famouri P. Piston rings friction comparison in a free piston and conventional crankshaft engines. In: Internal combustion engine division fall technical conference. American Society of Mechanical Engineers; 2018. V002T07A12.

[35] Yuan C, Xu J, He Y. Parametric study on the starting of a free-piston engine alternator. Int J Engine Res 2017;19(4):411–22.

[36] Rayl SC. The method of characteristics for irrotational flow of a semi-perfect gas. 1958.

[37] Winterbone DE, Turan A. Chapter 3 - engine cycles and their efficiencies. In: Winterbone DE, Turan A, editors. Advanced thermodynamics for engineers. second ed. Boston: Butterworth-Heinemann; 2015. p. 35–59.

[38] Hodgson M, Roy S, Roskilly AP, Smallbone A. The performance and efficiency of novel oxy-hydrogen-argon gas power cycles for zero emission power generation. Energy Convers Manag 2021;244:114510.

[39] Baker N, Jalal A, Wang J, Korbekandi RM. Experimental comparison of two linear machines developed for the free piston engine. J Eng 2019;2019(17):4406–10.

[40] Baker NJ. Linear generators for direct drive marine renewable energy converters. Durham University; 2003.

[41] Rathore SS, Mishra S, Paswan MK. A review on design and development of free piston linear generators in hybrid vehicles. In: IOP conference series: materials science and engineering. IOP Publishing; 2019, 012053.

[42] Subramanian J, Mahmudzadeh F, Bade M, Famouri P. Simulation and experimental validation of equivalent circuit parameters and core loss in a tubular permanent magnet linear generator for free piston engine applications. In: 2019 IEEE international electric machines & drives conference. IEMDC); 2019. p. 57–62.

[43] Wang J, Howe D, Lin Z. Comparative studies on linear motor topologies for reciprocating vapor compressors. In: IEEE international electric machines & drives conference. IEEE; 2007. p. 364–9. 2007.

[44] Korbekandi RM, Baker NJ, Kulan MC, Jalal AS, Wu D, Li M. Dynamic characteristics and demonstration of an integrated linear engine generator with alternative electrical machines. Energies 2022;15(14):5295.

[45] Baker N, Korbekandi RM, Jalal AS, Wu D. Performance of a tubular machine driven by an external-combustion free-piston engine. J Eng 2019;2019:3867–71.

[46] Korbekandi RM, Baker NJ, Kulan M, Wu D. Modelling and build of an integrated linear engine generator designed for power density. In: 2021 IEEE energy conversion congress and exposition (ECCE); 2021. p. 4103–10.

[47] McBride BJ, Zehe MJ, Gordon S. NASA Glenn coefficients for calculating thermodynamic properties of individual species: national Aeronautics and Space Administration. John H. Glenn Research Center; 2002.

[48] Dincer I, Rosen MA. In: Dincer I, Rosen MA, editors. Chapter 2 - exergy and energy analyses. Exergy. Amsterdam: Elsevier; 2007. p. 23–35.

[49] Jamnani MB, Kardgar A. Energy-exergy performance assessment with optimization guidance for the components of the 396-MW combined-cycle power plant. Energy Sci Eng 2020;8(10):3561–74.

[50] Dincer I, Rosen MA. Chapter 1 - thermodynamic fundamentals. In: Dincer I, Rosen MA, editors. Exergy. third ed. Elsevier; 2021. p. 1–22.

[51] Dincer I, Rosen MA. Chapter 1 - exergy and its ties to the environment, economics, and sustainability. In: Dincer I, Rosen MA, editors. Exergy analysis of heating, refrigerating and air conditioning. Boston: Elsevier; 2015. p. 1–42.

[52] Dincer I, Rosen MA. Chapter 2 - energy and exergy assessments. In: Dincer I, Rosen MA, editors. Exergy analysis of heating, refrigerating and air conditioning. Boston: Elsevier; 2015. p. 43–97.

[53] Rauch M, Mudrinić S, Galović A. Detailed analysis of exergy destruction of all basic types of heat exchangers. Processes 2022;10(2):249.

[54] Marmolejo-Correa D, Gundersen T. A comparison of exergy efficiency definitions with focus on low temperature processes. Energy 2012;44(1):477–89.

[55] Alabdoadaim MA, Agnew B, Potts I. Performance analysis of combined Brayton and inverse Brayton cycles and developed configurations. Appl Therm Eng 2006;26 (14):1448–54.

[56] Riazi H, Ahmed N. Effect of the ratio of specific heats on a small scale solar brayton cycle. Procedia Eng 2012;49:263–70.

[57] Boretti A. Towards 40% efficiency with BMEP exceeding 30bar in directly injected, turbocharged, spark ignition ethanol engines. Energy Convers Manag 2012;57: 154–66.

[58] Hoag K.L. An exploratory look at an aggressive miller cycle for high BMEP heavy-duty diesel engines. SAE Technical Paper 2019; 2019-01-0231.

[59] Trattner A, Grassberger H, Schoegl O, Schmidt S, Kirchberger R, Eichlseder H, et al. Advantages and challenges of lean operation of two-stroke engines for hand-held power tools. SAE International Journal of Engines 2015;8(1):101–19.

[60] Piecha P, Ninaus C, Schmidt S, Kirchberger R. Practicability and influencing factors of a lean burn mode for two-stroke engines in hand-held powertools. SAE Technical Paper; 2017.

[61] Hanipah MR, Mikalsen R, Roskilly AP. The real-time interaction model for transient mode investigations of a dual-piston free-piston engine generator. Appl Therm Eng 2022;212:118629.

[62] Zheng J, Caton JA. Second law analysis of a low temperature combustion diesel engine: effect of injection timing and exhaust gas recirculation. Energy 2012;38(1): 78–84.

[63] Kilicarslan A, Kiris M. Exergy destruction analysis of a gas turbine power plant. Hittite Journal of Science and Engineering 2018;5(4):339–46.

[64] Mrzljak V, Poljak I, Medica-Viola V. Energy and exergy efficiency analysis of sealing steam condenser in propulsion system of LNG carrier. NASE MORE: znanstveni časopis za more i pomorstvo 2017;64(1):20–5.